# Polarizable Six-Point Water Models from Computational and Empirical Optimization

Philipp Tröster, Konstantin Lorenzen, and Paul Tavan*

Lehrstuhl für Biomolekulare Optik, Fakultät für Physik, Ludwig-Maximilians-Universität München, Oettingenstrasse 67, D-80538 Müunchen, Germany

S *Supporting Information*

ABSTRACT: Tröster et al. (*J. Phys. Chem B* **2013**, *117*, 9486−9500) recently suggested a mixed computational and empirical approach to the optimization of polarizable molecular mechanics (PMM) water models. In the empirical part the parameters of Buckingham potentials are optimized by PMM molecular dynamics (MD) simulations. The computational part applies hybrid calculations, which combine the quantum mechanical description of a H_2O molecule by density functional theory (DFT) with a PMM model of its liquid phase environment generated by MD. While the static dipole moments and polarizabilities of the PMM water models are fixed at the experimental gas phase values, the DFT/PMM calculations are employed to optimize the remaining electrostatic properties. These properties cover the width of a Gaussian inducible dipole positioned at the oxygen and the locations of massless negative charge points within the molecule (the positive charges are attached to the hydrogens). The authors considered the cases of one and two negative charges rendering the PMM four- and five-point models TL4P and TL5P. Here we extend their approach to three negative charges, thus suggesting the PMM six-point model TL6P. As compared to the predecessors and to other PMM models, which also exhibit partial charges at fixed positions, TL6P turned out to predict all studied properties of liquid water at $p_0 = 1$ bar and $T_0 = 300$ K with a remarkable accuracy. These properties cover, for instance, the diffusion constant, viscosity, isobaric heat capacity, isothermal compressibility, dielectric constant, density, and the isobaric thermal expansion coefficient. This success concurrently provides a microscopic physical explanation of corresponding shortcomings of previous models. It uniquely assigns the failures of previous models to substantial inaccuracies in the description of the higher electrostatic multipole moments of liquid phase water molecules. Resulting favorable properties concerning the transferability to other temperatures and conditions like the melting of ice are also discussed.
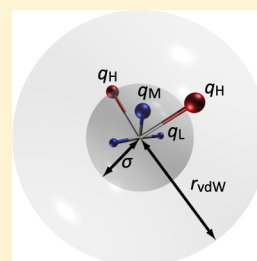
1. INTRODUCTION

Liquid water features many unusual properties and is the biologically most important solvent, because life originates from water.[1] Driven by the hope to understand, in most simple terms, the microscopic causes of the bulk liquid's very special properties, the development of simplified molecular energy functions, which can reproduce these properties as closely as possible in molecular dynamics (MD) simulations, is a long lasting and ongoing international effort.[2,3]

Accurate theoretical descriptions of molecular properties require quantum mechanical methods like density functional theory (DFT) or other approaches of quantum chemistry. Simulation systems addressing the bulk liquid should comprise several thousand water molecules[4−8] and corresponding MD simulations should cover several nanoseconds[9,10] for well-sampled computations of properties such as the dielectric constant. Here, DFT and other methods of quantum chemistry are excluded for reasons of computational manageability[11,12] and one must resort to less accurate but computationally much more efficient and preferentially polarizable[3,13] molecular mechanics (PMM) models.

The sketched dilemma between accuracy and computational efficiency can be partially circumvented, for instance, by the recent hybrid method of Schwörer et al.,[14] because it combines a PMM-MD treatment of almost all molecules in a liquid phase simulation system with a DFT treatment of a few. In a first application this novel technology has been exploited for the mixed computational and empirical optimization of three PMM model potentials featuring $\nu = 3$, 4, and 5 points of force action.[8]

The construction of these so-called[15] TLνP model potentials was driven by the conviction that quantitatively accurate descriptions of water in the liquid phase and in inhomogeneous condensed phase environments such as protein−solvent mixtures can only be achieved, if the physics of the individual molecules is represented as correctly as possible. For reasons of computational manageability, corresponding models should also be as simple as possible, of course. The question then is how complex a model must be made until it can start to cover the essential physics of a water molecule in a condensed phase environment with sufficient accuracy.

The TLνP models describe the electrostatic signature of the H_2O molecule by three ($\nu = 3$, 4) or four ($\nu = 5$) static partial charges, where two positive charges $q_H > 0$ are located at the hydrogens and the remaining negative charges either at the oxygen or in its vicinity, such that the static dipole moment has

the experimental gas phase value[16] μ_{exp}^g = 1.855 D for $v \geq 4$ and is 2.091 D for $v = 3$. They account for the polarizability α by a Gaussian inducible dipole $\boldsymbol{\mu}^i(r)$ of width σ, apply the experimental gas phase value[17] α_{exp}^g = 1.47 Å³, and model the van der Waals interactions by a Buckingham potential[18]

$$E_B(r) = A_1 \exp(-rA_2) - B/r^6 \qquad (1)$$

where r is the distance from the oxygen atom and (A_1, A_2, B) are positive parameters. Thus, $E_B(r)$ and the Gaussian inducible dipole $\boldsymbol{\mu}^i(r)$ are both centered at the oxygen. The three atomic masses of H_2O are arranged in the experimental liquid phase molecular geometry $\mathbf{G}_m^l$, which is given by[19,20] the bond angle φ_{HOH} = 105.3° and the bond length l_{OH} = 0.968 Å.

Just like other PMM three-point models,[21−25] the resulting TL3P potential did not render reasonable descriptions[8] of liquid water at the standard temperature T_0 = 300 K and experimental density[26] $n_{exp}(T_0,p_0)$ = 0.9965 g/cm³ assumed at the standard pressure p_0 = 1 bar. For instance, TL3P and related three-point PMM models overestimate the dielectric constant[27] $\epsilon(T_0,p_0)$ = 78 by about a factor 2, which is why we will exclude these models from our further discussions.

The TL4P and TL5P models, however, not only reproduced the few properties targeted by the empirical optimization but also rendered excellent predictions for a number of other bulk phase properties[8] at T_0 and $n_{exp}(T_0,p_0)$, which include ϵ, the diffusion coefficient D, the viscosity η, the heat capacity C_p at constant pressure, and the isothermal compressibility κ_T. A notable exception was the thermal expansion coefficient $\alpha_p(T_0,p_0) = -(\partial \ln n/\partial T)_p$, which is the negative temperature derivative of the density at constant pressure, has the experimental value[26] of 2.75×10^{-4} K⁻¹, and was overestimated by at least a factor of 2.

Concerning α_p, the performance of the TL4P and TL5P models is comparable to that of other four- and five-point PMM models,[28−34] which were optimized by exclusively empirical parameter searches. As a possible remedy Kiss and Baranyai[34] suggested to choose also the Lennard-Jones[35] parameters A and B as polarizable in a four-point "one-charge on spring" PMM model (called BKd3) featuring Gaussian partial charges. In a second attempt[36] they combined a nonpolarizable Buckingham potential with a four-point "three Gaussian charges on springs" PMM model (called BK3) representing a polarizability distributed on the three charges.

In both cases the parameter sets are larger than the eight numbers required to specify conventional PMM four-point models, because they additionally contain two response parameters and two Gaussian widths. Furthermore, the use of Gaussian partial charges implies an enhanced computational effort. After empirical optimizations, which included the dielectric constant and the temperature density function of liquid water (BKd3) or the densities of the liquid and of ice (BK3) as targets, both models managed to reproduce α_p at T_0 much better. BKd3 missed α_p by[37] only −11% and BK3 by +17%.

The BKd3 and BK3 deviations for α_p are larger than the corresponding 3% underestimate provided by the recent partially polarizable[38] and very complex model iAMOEBA,[39] whose 19 independent parameters were optimized using large numbers of experimental data on liquid water [including $\alpha_p(T_0,p_0)$ and $\epsilon(T_0,p_0)$] and of quantum chemical results on small icy clusters as targets. These deviations are similar to the 9% overestimate[37] characterizing the nonpolarizable[38] TIP4P/2005 model,[40] whose parameters (just like those of BKd3 and

iAMOEBA) were optimized using $\alpha_p(T_0,p_0)$ as one of the targets. On the other hand, TIP4P/2005 underestimates the dielectric constant[27] $\epsilon(T_0,p_0)$ by about 25% whereas the two PMM models BKd3 and BK3 as well as iAMOEBA yield close ($\pm 3\%$) matches also in this respect. Note that the non-polarizable TIP4Q model,[41] which features four partial point charges and has been parametrized with $\epsilon(T_0,p_0)$ and with the temperature-density profile $n(T,p_0)$ as optimization targets, manages to reproduce $\alpha_p(T_0,p_0)$ quite accurately and over-estimates $\epsilon(T_0,p_0)$ by only about 3%.

Because the quoted parametric PMM approaches[34,36] are based on different physical pictures with BKd3 emphasizing a field-dependence of the van der Waals interactions and with BK3 putting forward three distributed polarizabilities of the "Gaussian charges on springs"-type, the microscopic physical reason for the concurrent reproduction of $\epsilon(T_0,p_0)$ and $\alpha_p(T_0,p_0)$ remains unclear. Similarly, the complexity of iAMOEBA, which includes a molecular flexibility, a distributed but incomplete polarizability,[38] and atomic static multipoles as described by 19 adjustable parameters, prevents any identi-fication of those microscopic physical properties, which lead to reasonable liquid phase descriptions in some respects and to suboptimal ones in others. The quadrupole moments of an iAMOEBA molecular model, for instance, deviate by an average of 12% and the polarizability even by 24% from the respective experimental values,[39] demonstrating that iAMOEBA is an effective[38] but not a physical model for water. Similar considerations apply to other nonpolarizable and effective model potentials like TIP4P/2005[40] or TIP4Q[41] (despite their much smaller complexity).

In contrast, the mixed computational and empirical approach toward the optimization of water models suggested in ref 8 opens the chance to identify the microscopic physical causes for the joint match of $\epsilon(T_0,p_0)$ and $\alpha_p(T_0,p_0)$, because it is based on experimentally or theoretically well-established physical proper-ties of individual water molecules, because it clearly distinguishes between electrostatic and van der Waals interactions, and because it applies separate and conceptually different methods to the choice or optimization of the associated model parameters. Concerning the electrostatics, the well-known[16,17] dipole moment μ_{exp}^g and polarizability α_{exp}^g of an isolated water molecule as well as the liquid phase geometry[19,20] $\mathbf{G}_m^l$ are employed as invariant cornerstones of the model construction. The widths σ of the Gaussian inducible dipole distribution $\boldsymbol{\mu}^i(r)$ centered at the oxygen and the spatial distribution of the negative partial charges within the molecule, which characterize the electrostatic signature of the respective model, are determined by DFT/PMM calculations. Solely the three van der Waals parameters (A_1, A_2, B) are eventually obtained by empirical optimization.

1.1. Significance of a TL6P Model. Suppose now that a slightly more complex PMM model, which solely extends the TL5P electrostatics by one additional negative charge, is parametrized by the same approach,[8] and therefore, will be called TL6P, could concurrently reproduce ϵ and α_p. Then such a success would prove that the incorrect electrostatic signatures of the predecessor models TL4P and TL5P are the cause for the noted failures of these and related[28−34] PMM models. In particular, it would demonstrate that neither polarizable van der Waals potentials[34] nor distributed polarizabilities[36,39] are necessary for remedying the shortcomings of PMM four- and five-point models concerning α_p. The check of this possibility is the key objective of this paper.

The successful outcome of this check, which will be described below, has inspired us to a follow-up study,[42] which by some strange fortune happened to be published before the current manuscript was accepted for publication. Based on 20 ns replica exchange molecular dynamics simulations, this follow-up study demonstrates that the accurate TL6P value calculated for the negative density derivative $\alpha_p(T_0,p_0)$ even translates into a remarkably accurate prediction of the whole temperature density profile $n(T,p_0)$ in the range $T \in [250, 320]$ K by TL6P, whereas TL4P and TL5P grossly fail in this respect. As explained in ref 42, this progress sheds light on the microscopic physical cause for the density maximum of liquid water. Thus, the construction and properties of the polarizable six-point model TL6P and the differences to the less complex predecessor models are now even of an enhanced interest.

As follows from Figure 1, the electrostatic signature of the six-point PMM model TL6P is given by the parameter set $\Lambda_{e,6}$
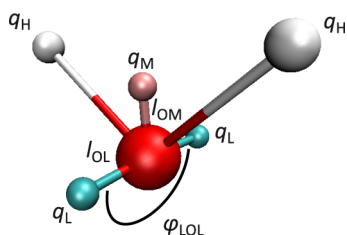

Figure 1. Electrostatic signature of the TL6P model defined by the liquid phase molecular geometry G_m^l, by the distance l_{OM} between the red oxygen atom O and the pink massless point M, whose charge $q_M < 0$ is located on the bisectrix of the HOH triangle, by the distance l_{OL} between O and each of the cyan massless points L, which carry charges $q_L < 0$ and form a triangle LOL perpendicular to the molecular plane, whose bisectrix coincides with that of the HOH triangle, and by the angle φ_{LOL}.

$= \{q_M, l_{OM}, l_{OL}, \varphi_{LOL}\}$. TL6P carries, beyond the partial charges $q_H > 0$ at the hydrogen atoms, negative partial charges $q_{M/L}$ at the massless points M and L. The electrostatic neutrality of the molecule dictates that

$$q_M + 2q_L + 2q_H = 0 \tag{2}$$

Matching one of the corner stones of the parametrization, the charges q_H, q_M, and q_L must additionally reproduce the experimental gas phase dipole moment

$$\mu_{exp}^g = 2q_H h_{HOH} + q_M l_{OM} - 2q_L h_{LOL} \tag{3}$$

where $h_{HOH} = l_{OH} \cos(\varphi_{HOH}/2)$ and $h_{LOL} = l_{OL} \cos(\varphi_{LOL}/2)$ are the heights of the HOH- and LOL-triangles, respectively. According to eqs 2 and 3 only one of the charges, e.g., q_M, can be independently chosen, if the geometric quantities l_{OM}, l_{OL}, and φ_{LOL} are considered as further independent parameters. For $q_M = 0$ the six-point model TL6P reduces to a five-point model with the electrostatic parameters $\Lambda_{e,5} \equiv \{l_{OL}, \varphi_{LOL}\}$ and for $q_L = 0$ to a four-point model with the single parameter $\Lambda_{e,4} \equiv \{l_{OM}\}$.

1.2. DFT/PMM Scheme of TLνP Electrostatics Optimization. According to the scheme of parameter optimization, which is explained in great detail in ref 8, the electrostatic parameters $\Lambda_{e,\nu}$ and the Gaussian widths σ of such ν-point PMM models are determined by DFT/PMM calculations. Here for each ν-point PMM potential an ensemble $\mathcal{S}$ consisting of liquid phase structural snapshots s is generated by PMM-MD

simulations, which are executed at T_0 and at the experimental density $n_{exp}(T_0,p_0)$ for a constant number N of TLνP models enclosed by a periodic volume V. In subsequent one-point DFT/PMM hybrid calculations on the snapshots $s \in \mathcal{S}$, one of the water molecules is selected as the DFT fragment of the hybrid system such that the remaining PMM fragment represents a spot check of a liquid phase environment.

In this way, DFT/PMM predictions on electrostatic properties of water molecules are determined, which should be representative for aqueous environments at the given conditions. These properties cover the dipole moments $\mu_{DFT/PMM}(s)$ of the DFT fragments and the electrostatic potentials $\Phi(r|\rho_s)$, which are caused by their electron densities ρ_s at points $r \in \mathcal{P}$ randomly selected from surrounding spherical surfaces $\mathcal{P}$.

First, the induced dipole moments

$$\mu_{DFT/PMM}^i(s) \equiv \mu_{DFT/PMM}(s) - \mu_{DFT} \tag{4}$$

where μ_{DFT} is the dipole moment of an isolated DFT water molecule at the liquid phase geometry ($|\mu_{DFT}|$ = 1.79 D), are employed to optimize the width σ of the induced Gaussian PMM dipole. To this aim the $\mu_{DFT/PMM}^i(s)$ are compared with the linear responses[8,43]

$$\mu_\sigma^i(s) \equiv \alpha_{DFT}^g \langle \mathbf{E}(s) \rangle_\sigma \tag{5}$$

of Gaussian inducible dipoles of the polarizability α_{DFT}^g = 1.58 Å³, which are placed at the positions of the oxygen atoms within the respective DFT fragments of the snapshots $s \in \mathcal{S}$. These oxygen atoms are located at the origin of the coordinate system and the brackets $\langle ... \rangle_\sigma$ in eq 5 denote the Gaussian average

$$\langle f \rangle_\sigma = \frac{1}{(2\pi\sigma^2)^{3/2}} \int d^3r'\, f(r')\, \exp[-r'^2/2\sigma^2]$$

of a function $f(\mathbf{r})$ around that origin. In eq 5 this function is the electric field $\mathbf{E}(\mathbf{r}|s)$, which is generated by the PMM water models surrounding in the chosen snapshot s the selected DFT fragment. The optimal width σ of the Gaussian dipole then follows from optimizing the correlations between the compared data $\mu_{DFT/PMM}^i(s)$ and $\mu_\sigma^i(s)$.

Next, the values $\Phi(r|\rho_s)$ of the surface potential serve to compute optimized electrostatic signatures. For this purpose the potential $\Phi[r|\mu_\sigma^i(s)]$, which is generated by the induced Gaussian dipole of a PMM model replacing the DFT fragment in each snapshot $s \in \mathcal{S}$, is subtracted from the DFT/PMM potential $\Phi(r|\rho_s)$ of the DFT fragment at all points $r \in \mathcal{P}$, yielding a set of values $\Phi(r|\rho_s^{stat})$. This set serves as a mean field template for the static part of the PMM surface potential $\Phi(r|\Lambda_{e,\nu})$, which is determined by the electrostatic signature $\Lambda_{e,\nu}$. The optimal parameters $\Lambda_{e,\nu}^{opt}$ then follow by minimizing for all $s \in \mathcal{S}$ and all $r \in \mathcal{P}$ the root-mean-square deviation (RMSD)

$$\zeta(\Lambda_{e,\nu}) \equiv \sqrt{\langle [\Phi(r|\rho_s^{stat}) - \Phi(r|\Lambda_{e,\nu})]^2 \rangle_{\mathcal{S},\mathcal{P}}} \tag{6}$$

with respect to the parameters $\Lambda_{e,\nu}$.

1.3. Empirical Optimization of the van der Waals Interactions. As soon as the electrostatic parameters σ and $\Lambda_{e,\nu}$ are determined, the three parameters of the Buckingham potential eq 1 are empirically optimized by weak-coupling[44] NVT MD simulations executed at at T_0 and $n_{exp}(T_0,p_0)$. Here the targets for A_1, A_2, and B are the position r_1 of the first peak

of an experimental[45−48] oxygen−oxygen radial distribution function (RDF) $g_{OO}(r)$, the standard pressure of $p_0 = 1$ bar, and the experimental[49,50] potential energy $E_{pot}(T_0,p_0) = -9.92$ kcal/mol per molecule, respectively. The sketched computational and empirical steps of parameter optimization are repeated until self-consistency is reached.

The Buckingham parameters A_1 of the TL4P and TL5P models were optimized[8] to match the value $r_1 = 2.76$ Å given by the RDF of Soper.[46] The recent data of Skinner et al.,[48] however, suggest the 1.5% larger value $r_1 = 2.80$ Å. It is unknown how strongly the properties of resulting TLνP models are affected by such a slight change of the target value for A_1. This is one of the minor questions, which we will also address below, by additionally adjusting the Buckingham parameter A_1 of an alternative TL6P model to the most recent[48] RDF. Correspondingly, we will call this alternative model TL6P^{Sk}.

2. METHODS AND SIMULATIONS

The self-consistent scheme of mixed computational and empirical parameter optimization and the various methods and simulations applied to the construction and evaluation of PMM water models are motivated and explained in sections 2 and 3 of ref 8. Apart from a few slight modifications we have exactly copied all these procedures for the construction of the six-point models TL6P and TL6P^{Sk} introduced above. Therefore, the given reference and a short sketch of the copied procedures must suffice in combination with an outline of the few modifications.

2.1. Parameter Optimization. Just like for TL4P and TL5P also the TL6P and TL6P^{Sk} simulation systems, which were employed during the parametrization cycles, contained $N_m = 1500$ water models. Here, $N_m VT$ PMM-MD simulations were executed at $T = T_0$ and $n_{exp}(T_0,p_0)$ with the parallelized program package IPHIGENIE[51] taking advantage of its efficient fast multipole treatment of the electrostatics,[51−54] of its toroidal boundary conditions,[9] and of its moving-boundary reaction field correction[55] for the long-range electrostatics (for further details on the electrostatics computation see section S1 in the Supporting Information). For each of the two TL6P models they served to generate the ensembles $\mathcal{S}$ covering 1000 liquid phase snapshots s for the PMM/DFT calculations. The same conditions were also applied to the weak-coupling simulations[44] aiming at the Buckingham parameters. The PMM/DFT calculations were again executed with the interface[14,56] between IPHIGENIE and the grid-based DFT program CPMD[57] using the same functionals,[58,59] pseudopotential,[60] and 80 Ry plane-wave cutoff as for TL4P and TL5P.[8]

The dipole moments $\boldsymbol{\mu}_{DFT/PMM}(s)$ and the electrostatic surface potentials $\Phi(\mathbf{r}|\rho_s)$ of the DFT fragments belonging to the ensembles $\mathcal{S}$ were then employed to optimize the widths σ and parameter sets $\Lambda_{e,6}$ characterizing the electrostatic signatures of the two TL6P models by the procedures developed in ref 8. As compared to TL5P, each parameter set $\Lambda_{e,6}$ contains four instead of only two parameters, such that a four-dimensional space had to be scanned for the minimization of the deviation functional $\zeta(\Lambda_{e,6})$ defined by eq 6. Here q_M was scanned in the range $[-0.65, -0.35]$ e with steps of 0.0001 e, the distances l_{OM} and l_{OM} in the range $[0.0, 0.7]$ Å with the steps $\Delta l = 0.001$ Å, and the angle φ_{LOL} in the range $[0, 360]°$ with the steps $\Delta\varphi_{LOL} = 1°$.

2.2. New Observables for Quality Control. In the presentation of the quality, by which the surface potential $\Phi(\mathbf{r}|\Lambda_{e,\nu})$ of the respective ν-point model matches the

associated ensemble average DFT/PMM reference potential $\langle\Phi(\mathbf{r}|\rho_s^{stat})\rangle_S$ on all points $\mathbf{r} \in \mathcal{P}$, it is advantageous to employ instead of the RMSD $\zeta(\Lambda_{e,\nu})$ given by eq 6 a more direct dimensionless measure. If the values of the potentials are given with respect to the molecular frame of reference, then $\zeta(\Lambda_{e,\nu})$ is related through

$$\xi^2(\Lambda_{e,\nu}) = \zeta^2(\Lambda_{e,\nu}) - \sigma_S^2 \tag{7}$$

to the RMSD

$$\xi(\Lambda_{e,\nu}) \equiv \sqrt{\langle[\langle\Phi(\mathbf{r}|\rho_s^{stat})\rangle_S - \Phi(\mathbf{r}|\Lambda_{e,\nu})]^2\rangle_{\mathcal{P}}} \tag{8}$$

of the values of the model potential $\Phi(\mathbf{r}|\Lambda_{e,\nu})$ from the values of the ensemble average surface potential $\langle\Phi(\mathbf{r}|\rho_s^{stat})\rangle_S$ measured at all points $\mathbf{r} \in \mathcal{P}$ and to the average variance

$$\sigma_S^2 \equiv \langle[\Phi(\mathbf{r}|\rho_s^{stat}) - \langle\Phi(\mathbf{r}|\rho_s^{stat})\rangle_S]^2\rangle_{S,\mathcal{P}} \tag{9}$$

of the DFT/PMM potential values $\langle\Phi(\mathbf{r}|\rho_s^{stat})\rangle$ within the snapshot ensemble $\mathcal{S}$, where the average extends over all points $\mathbf{r} \in \mathcal{P}$. The standard deviation

$$\sigma_{\mathcal{P}} \equiv \sqrt{\langle[\langle\Phi(\mathbf{r}|\rho_s^{stat})\rangle_S - \langle\langle\Phi(\mathbf{r}|\rho_s^{stat})\rangle_S\rangle_{\mathcal{P}}]^2\rangle_{\mathcal{P}}} \tag{10}$$

of the ensemble average values $\langle\Phi(\mathbf{r}|\rho_s^{stat})\rangle_S$ of the DFT/PMM surface potential with respect to all points $\mathbf{r} \in \mathcal{P}$ then characterizes for $\langle\Phi(\mathbf{r}|\rho_s^{stat})\rangle_S$ the dynamical range of variations on the surrounding surface and, therefore, defines a scale on which the standard deviations σ_S and the RMSD $\xi(\Lambda_{e,\nu})$ can be measured by the dimensionless quantities $\sigma_S/\sigma_{\mathcal{P}}$ and $\xi(\Lambda_{e,\nu})/\sigma_{\mathcal{P}}$, respectively.

2.3. Evaluation of the TL6P Models. To evaluate the quality of the resulting TL6P and TL6P^{Sk} models by comparisons with relevant experimental data, we applied the methods described in ref 8 and calculated the same molecular and bulk phase observables that were previously evaluated for the TLνP models with $\nu \leq 5$.

The bulk properties at T_0 and $n_{exp}(T_0,p_0)$ were obtained from PMM-MD simulations with durations and settings identical to the ones enumerated in Tables 2 and 3 of ref 8 for three different system sizes N_s, N_m, and N_l. While the numbers $N_s = 728$ and $N_m = 1500$ of molecular models in the small and intermediately sized periodic boxes were chosen identical, the large boxes contained this time $N_l = 5300$ instead of only 3374 molecular models. Thus, we carried out $N_i V_i T_0$ simulations, $i \in \{s, m, l\}$, with durations of 1.5−4.5 ns at the experimental density $n_{exp}(T_0,p_0)$ and at slightly varied densities $n_\pm = (1 \pm 0.05)n_{exp}$ applying Bussi[61] and minimally invasive (MI) Berendsen thermostats.[62] Furthermore, we carried out $N_i p_0 T_0$ and $N_s p_0 T_\pm$ simulations ($T_\pm = T_0 \pm 10$ K) for similar time spans controlling the pressure by a slowly coupled (10 ps) Berendsen barostat.[63]

The evaluated molecular properties cover the quadrupole moments of the monomers and the geometries $\mathbf{G}_d$, potential energies $E_{pot,d}$, and dipole moments μ_d of the dimers. Among the bulk phase observables are those that were targets of the empirical optimization, i.e., the average potential energy per molecule $\langle E_{pot}\rangle$ and the average pressure $\langle p\rangle$, and a series of other observables,[8] for which the computational results represent predictions. These are the average density $\langle n\rangle$ (from the $N_i p_0 T_0$ simulations), the dielectric constant ϵ (from the fluctuations of the total dipole moment in the $N_i V_i T_0$ simulations), the self-diffusion coefficient D and viscosity ν (from the size dependence[4] of D observed by means of the

$N_i V_i T_0$[MI] simulations), the isothermal compressibility κ_T (from the $N_s V_s T_0$ simulations), and the heat capacity C_p and the thermal expansion coefficient α_p (from the $N_s p_0 T_\pm$ simulations).

According to our original design of this study, the evaluation of the TL6P models should be restricted to the liquid phase standard conditions T_0 and p_0. The capability to predict also liquid phase properties at other conditions, e.g., the temperature profiles $n(T,p_0)$ of the density, $\alpha_p(T,p_0)$ of the thermal expansion coefficient, $\Delta H_{vap}(T,p_0)$ of the heat of vaporization, and $C_p(T,p_0)$ of the heat capacity, was planned for a possible follow-up study, which we wanted to tackle in the case of a favorable outcome of the present study. These data are meanwhile presented and discussed in ref 42 and in the associated Supporting Information. Following reviewer requests we have, however, included in the current study further information on gas phase and solid state properties like the second virial coefficient $B_2(T)$ and the melting temperature T^m of ice Ih. The computational methods applied in these additional simulation studies are described in sections S7 (B_2) and S10 (T^m) of the Supporting Information, which present and discuss also the associated results. The following text will take up these issues of transferability to other than standard liquid phase conditions solely in a condensed and summarizing form in section 4.3.

3. RESULTS

Before presenting the molecular and bulk phase properties of the TL6P and TL6P^{Sk} models resulting from the mixed computational and empirical optimization, we address a remarkable peculiarity of these six-point models, which became apparent through the DFT/PMM optimization of their electrostatic signatures.

3.1. Quality of the Electrostatic DFT/PMM Refinement. First the correlations between the DFT/PMM and PMM induced dipole moments $\boldsymbol{\mu}^i_{DFT/PMM}(s)$ (eq 4) and $\boldsymbol{\mu}^i_\sigma(s)$ (eq 5) were employed to optimize the widths σ resulting in the values 0.806 Å for TL6P and 0.802 Å for TL6P^{Sk}. The resulting optimal correlations are depicted by Figure S4 in section S2 of the Supporting Information. The access to optimized widths σ is a prerequisite for the DFT/PMM calculation of the electrostatic signatures $\Lambda_{e,6}$.

As explained above in connection with eq 6, the parameters $\Lambda_{e,6}$ characterizing the electrostatic signatures of the TL6P models are optimized by comparing the zero-field potential $\Phi(\mathbf{r}|\Lambda_{e,6})$ of the respective model with the supposedly static parts $\Phi(\mathbf{r}|\rho_s^{stat})$ of the potentials $\Phi(\mathbf{r}|\rho_s)$, which are generated by the electron densities ρ_s of the DFT fragments in liquid phase snapshots $s \in \mathcal{S}$ at points $\mathbf{r} \in \mathcal{P}$ on spherical surfaces surrounding the fragments. Here, the supposedly static parts are calculated for all $s \in \mathcal{S}$ as differences

$$\Phi(\mathbf{r}|\rho_s^{stat}) = \Phi(\mathbf{r}|\rho_s) - \Phi[\mathbf{r}|\mu^i_\sigma(s)]$$

between the potentials $\Phi[\mathbf{r}|\mu^i_\sigma(s)]$ of induced Gaussian dipoles $\boldsymbol{\mu}^i_\sigma(s)$ at the positions of the respective DFT fragment's oxygen atom and the DFT surface potentials $\Phi(\mathbf{r}|\rho_s)$. The addressed comparison is effected by means of the RMSD $\zeta(\Lambda_{e,6})$ defined by eq 6.

Now it is interesting to check, whether the supposedly static parts $\Phi(\mathbf{r}|\rho_s^{stat})$ of the DFT/PMM potentials $\Phi(\mathbf{r}|\rho_s)$ are actually static. Using the DFT fragment's molecular frame of reference, we have therefore calculated the average values

$\langle\Phi(\mathbf{r}|\rho_s^{stat})\rangle_S$ and the variances $\sigma_S^2(\mathbf{r})$ of the values $\Phi(\mathbf{r}|\rho_s^{stat})$ within $\mathcal{S}$ not only for the two TL6P potentials but also for their TL5P and TL4P predecessors. Averaging over all points $\mathbf{r} \in \mathcal{P}$ and taking the square root then yielded the standard deviations σ_S defined by eq 9, which measure the average sizes of the fluctuations in the ensembles $\mathcal{S}$ of potential values $\Phi(\mathbf{r}|\rho_s^{stat})$. If these potentials should be actually static, as assumed by the construction of the TLvP models ($v = 4, 5, 6$), then the σ_S should be very small as compared to the variations of the ensemble average potentials $\langle\Phi(\mathbf{r}|\rho_s^{stat})\rangle_S$ on the spherical surfaces. The sizes of these variations are measured by the quantities $\sigma_\mathcal{P}$ defined by eq 10.

Table 1 lists the resulting standard deviations σ_S in units of $\sigma_\mathcal{P}$. Apparently, the fluctuations σ_S of the snapshot potentials

Table 1. Standard Deviations σ_S and RMSDs $\xi(\Lambda_{e,v}^{opt})$ Measured on the Scales $\sigma_\mathcal{P}$ As Defined by Eqs 8−10 of the Optimal TLvP Models

model	TL6P	TL6P^{Sk}	TL5P	TL4P
$\sigma_S/\sigma_\mathcal{P}$ [%]	0.2	0.2	0.3	0.3
$\xi(\Lambda_{e,v}^{opt})/\sigma_\mathcal{P}$ [%]	2.1	2.0	5.7	7.9

$\Phi(\mathbf{r}|\rho_s^{stat})$ are smaller than 0.3% of the total variation $\sigma_\mathcal{P}$ of the respective average surface potentials $\langle\Phi(\mathbf{r}|\rho_s^{stat})\rangle_S$. Thus, the supposedly static parts $\Phi(\mathbf{r}|\rho_s^{stat})$ of the DFT/PMM potentials $\Phi(\mathbf{r}|\rho_s)$ are nearly static, proving that one of the key assumptions of our procedure for model constructions is valid.

Table 1 additionally lists the RMSDs $\xi(\Lambda_{e,v}^{opt})$ between the surface potential values $\Phi(\mathbf{r}|\Lambda_{e,v}^{opt})$, which are generated by the optimized electrostatic signatures $\Lambda_{e,v}^{opt}$ of the TLvP models, and the ensemble average potential values $\langle\Phi(\mathbf{r}|\rho_s^{stat})\rangle_S$. Because of eq 7 and because the σ_S are small, these RMSDs $\xi(\Lambda_{e,v}^{opt})$ are almost identical to the optimization functionals $\zeta(\Lambda_{e,v}^{opt})$, which additionally shows that our optimization actually aims at the average DFT/PMM surface potential $\langle\Phi(\mathbf{r}|\rho_s^{stat})\rangle_S$.

Interestingly, the RMSDs $\xi(\Lambda_{e,6}^{opt})$ of the six-point models are by factors of about 3 and 4 smaller than those of the five- and four-point models, respectively. Hence, the six-point models represent the static part $\langle\Phi(\mathbf{r}|\rho_s^{stat})\rangle_S$ of the DFT/PMM mean field surface potential substantially better than their electrostatically less complex predecessors.

As shown above, in our construction of the TLvP models we have taken the DFT/PMM liquid phase quantity $\langle\Phi(\mathbf{r}|\rho_s^{stat})\rangle_S$ as the reference for the optimization of the electrostatic signatures $\Lambda_{e,v}$. Now one may ask how much this quantity differs from the surface potential $\Phi(\mathbf{r}|\rho^{vac})$, which is generated by the electron density ρ^{vac} of an isolated water molecule and is calculated, using the liquid phase geometry $\mathbf{G}_m^l$, by the same DFT approach. This question can be answered by replacing in eq 8 the PMM potential $\Phi(\mathbf{r}|\Lambda_{e,v})$ by the DFT potential $\Phi(\mathbf{r}|\rho^{vac})$ and by evaluating the new RMSD $\xi(\rho^{vac})$ between $\Phi(\mathbf{r}|\rho^{vac})$ and $\langle\Phi(\mathbf{r}|\rho_s^{stat})\rangle_S$ at the surface points $\mathbf{r} \in \mathcal{P}$.

We found that $\xi(\rho^{vac})$ is only 0.4% of the total variation $\sigma_\mathcal{P}$ of $\langle\Phi(\mathbf{r}|\rho_s^{stat})\rangle_S$; i.e., the differences between this average liquid phase potential and the vacuum result $\Phi(\mathbf{r}|\rho^{vac})$ are very small. Nevertheless, such differences exist and can be characterized by taking $\Phi(\mathbf{r}|\rho^{vac})$ as a reference for the optimization of $\Lambda_{e,v}$. Some of the resulting vacuum model parameters (q_M, φ_{LOL}) turn out to be identical to the liquid phase result, whereas others (l_{OM}, l_{OL}) increase by 2−3% (data not shown). Thus, the enhanced computational effort of employing DFT/PMM liquid phase ensembles has not been completely superfluous.

Table 2. TL6P Parameters Compared to Those of Their Predecessors[8]

model	$l_{OM}{}^a$	$l_{OL}{}^a$	$\varphi_{LOL}{}^b$	$q_H{}^c$	$q_M{}^c$	$q_L{}^c$	σ^a	$A_1{}^d$	$A_2{}^e$	B^f
TL6P	0.38	0.46	175	0.51	−0.57	−0.22	0.80	2.9	4.0	6.6
TL6P^{Sk}	0.39	0.46	173	0.51	−0.57	−0.22	0.80	3.0	4.0	6.3
TL5P		0.32	268	0.53		−0.53	0.85	0.6	3.4	11.8
TL4P	0.24			0.56	−1.12		0.84	0.8	3.6	9.9

^{a}Å. ^{b}deg. $^c e$. $^d 10^5$ kcal/mol. ^{e}Å^{-1}. $^f 10^2$ (Å^6 kcal)/mol.

Having ascertained the strongly enhanced quality, by which the electrostatic signatures $\Lambda_{e,6}$ match the DFT/PMM reference, we can now turn to the resulting molecular and bulk phase properties. Assuming that the DFT/PMM approach yields accurate descriptions, the properties obtained with TL6P should represent the experimental findings much better than the ones found[8] for the less complex predecessors.

3.2. Properties of the TL6P Potentials. Table 2 lists the final parameters $\lambda \in \Lambda_{e,6} \cup \{\sigma\} \cup \{A_1, A_2, B\}$ obtained for the two TL6P models by the iterative optimization scheme described in detail in ref 8 and sketched further above. Additionally, these parameters are compared with those of the preceding TL5P and TL4P models. The shown values are rounded. A table containing all relevant digits is provided for the TL6P models by section S3 of the Supporting Information. This section additionally gives parameters of Lennard-Jones potentials, which are almost equivalent to the TL6P Buckingham potentials.

3.2.1. Electrostatic Signatures from DFT/PMM. As explained by Figure 1, the electrostatic geometry of the TL6P models is defined by the distances l_{OM} and l_{OL} of the massless charge sites M and L from the oxygen atom O and by the angle φ_{LOL} spanned by the two massless "lone pair" sites L with respect to the center O. Figure 1 actually represents the optimized TL6P values specified in Table 2. Because the electrostatic parameters of TL6P and TL6P^{Sk} are almost identical, Figure 1 equally represents the latter model.

The angle φ_{LOL} of the TL6P models is smaller than 180° such that the projection of the points $\mathbf{r}_L$ onto the molecular plane falls slightly outside the molecular HOH-triangle on its bisectrix at a distance of 0.02 Å from $\mathbf{r}_O$. For TL5P, in contrast, the projection is 0.22 Å inside. Furthermore, for TL6P the distance l_{OL} is larger and the absolute value $|q_L|$ of the charge smaller than for TL5P.

An interesting feature of each of the two TL6P models is the very large distance l_{OM} of the site M from the oxygen atom (cf. Table 2). It is by about 60% larger than the corresponding distance in TL4P, which is moreover quite typical for PMM four-point models.[28−32,64] On the other hand, the absolute value $|q_M|$ of the associated TL6P charge is by about a factor 2 smaller than its four-point counterpart such that in TL6P the total negative charge is about evenly distributed among the M and combined L sites. Because q_M is small and l_{OM} large, the M site contributes only 30% to the 1.855 D static dipole moment of TL6P. Here we stress that it is this unexpected distribution of static partial charges within TL6P, that generates the favorable match of surface potentials discussed above in section 3.1.

In light of other nonpolarizable[66,67] and polarizable[65,68] six-point models, the electrostatic TL6P geometry represents a surprise. As is illustrated in Figure 2, the empirically optimized SWM6 model,[65] for instance, features a short l_{OM} distance (0.247 Å) and a large negative q_M charge (−1.133 e), which are both typical for PMM four-point models, and a very small angle
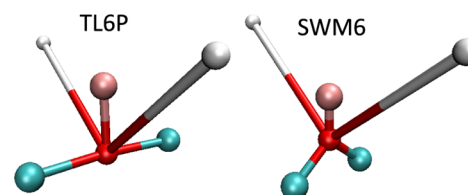

Figure 2. Electrostatic geometries of the two PMM six-point models TL6P and SWM6.[65]

$\varphi_{LOL} = 101°$ combined with small negative charges $q_L = -0.11\ e$ and small distances $l_{OL} = 0.315$ Å. In the zero-field case SWM6 additionally has a net positive charge of 0.288 e at O, because the negative charge of the Drude particle attached to O is overcompensated by the positive charge of O. As a result SWM6 has seven charge centers, for which Coulomb interactions have to be calculated. The complex PMM six-point model suggested by Wang et al.,[68] on the other hand, features an angle φ_{LOL}, which resembles that of TL5P and yields a projection of the L sites inside the HOH triangle on the bisectrix 0.231 Å distant from $\mathbf{r}_O$. Furthermore, the distance l_{OM} is by 24% smaller than that of TL6P. Thus, one of these models resembles TL4P and the other a mixture of TL4P and TL5P but none TL6P.

3.2.2. Widths of the Gaussian Inducible Dipoles from DFT/PMM. The Gaussian widths σ for the TL6P models, which are listed in Table 2, were given above in section 3.1 and derived by optimizing the PMM and DFT/PMM dipole correlations in section S2 of the Supporting Information. They are a little smaller than those of TL4P and TL5P. This decrease should cause slightly enhanced induced dipole interactions at small distances.

3.3.3. Buckingham Parameters from Empirical Optimizations. Much more significant are the differences among the listed Buckingham parameters. By construction also the two TL6P models differ in this respect. Recall that the target $r_1 = 2.76$ Å, which is the position of the first peak in Soper's[46] RDF $g_{OO}(r)$ and was weakly coupled to A_1 during the optimization of TL6P, was exchanged by the value[48] $r_1 = 2.80$ Å to yield TL6P^{Sk}. Correspondingly, the TL6P^{Sk} value of A_1 is about 5% larger and the value of B by as much smaller than the corresponding TL6P values. Thus, the 1.5% difference of the targets r_1 has translated into 5% differences of A_1 and B. Remarkably, the RDFs of the two TL6P models, which are depicted in Figure S8 of the Supporting Information, are almost identical at distances larger than about 3.0 Å and show differences only well within the first peak, indicating that the noted differences of A_1 and B solely affect the first solvation shells of the simulated liquids.

Much larger are the differences among the Buckingham potentials for TLνP models of different complexity. According to Table 2 the TL4P and TL5P potentials show some similarity but both strongly differ from the TL6P potential. The latter exhibit a much steeper and more short-range repulsion than the

former, as is witnessed by the much larger values of A_1 and A_2. The dispersion attraction, on the other hand, whose strength is measured by B, becomes smaller by a factor of almost 2 in the transition from TL4P and TL5P to the six-point case.

3.2.4. Quadrupole Moments from DFT/PMM. In section 3.1 we have seen that the potential $\Phi(\mathbf{r}|\rho^{\mathrm{vac}})$ generated by an isolated DFT water molecule on a surrounding spherical surface deviates from its DFT/PMM liquid phase relative $\langle\Phi(\mathbf{r}|\rho_s^{\mathrm{stat}})\rangle_S$ by an RMSD of only 0.4% as measured by the variation $\sigma_{\mathcal{P}}$ of $\langle\Phi(\mathbf{r}|\rho_s^{\mathrm{stat}})\rangle_S$ (cf. section 2.2). The main contributions to these surface potentials should be due to the quadrupole moments of the DFT and average DFT/PMM charge densities ρ^{vac} and $\langle\rho^{\mathrm{stat}}\rangle$, respectively. Thus, these quadrupole moments should be quite similar. However, because the DFT/PMM surface potentials $\langle\Phi(\mathbf{r}|\rho_s^{\mathrm{stat}})\rangle_S$ served as the references in the optimizations of TL6P electrostatic signatures $\Lambda_{\mathrm{e},6}$, the quadrupole moments of an isolated DFT water molecule should also closely resemble those of the TL6P models.

Table 3 confirms this expectation. Here, the comparison of the DFT vacuum result with the TL6P quadrupole moments is

Table 3. Quadrupole Moments of TL6P and of Other PMM Water Models, Which Are Given with Respect to the Center of Mass, Compared with Results of a DFT Vacuum Description and with Experimental Gas Phase Data through the Associated RMSDs R_{DFT} and R_{exp} As Measured by the Standard Deviation $\sigma_{\mathrm{exp}} = 2.1$ DÅ of the Gas Phase Data

	Q_{xx}/DÅ	Q_{yy}/DÅ	Q_{zz}/DÅ	$R_{\mathrm{DFT}}/\sigma_{\mathrm{exp}}$	$R_{\mathrm{exp}}/\sigma_{\mathrm{exp}}$
exp[69]	−0.13	2.63	−2.50	3.6%	
DFT$^{\mathrm{vac}}$	−0.19	2.59	−2.39		3.6%
TL6P	−0.18	2.59	−2.41	0.6%	3.0%
TL6P$^{\mathrm{Sk}}$	−0.19	2.59	−2.40	0.2%	3.4%
TL5P[8]	−0.11	2.53	−2.42	2.7%	3.4%
TL4P[8]	−0.29	2.53	−2.24	5.4%	9.0%
SWM6[65]	−0.30	2.39	−2.09	10.5%	14.0%

handily expressed by the associated RMSD R_{DFT} measured on the scale σ_{exp}, which is given by the variations among the values of the elements of the experimental[69] quadrupole tensor.

For the TL6P models R_{DFT} is less than 1% of σ_{exp} and, thus, is of the same order of magnitude as the 0.4% deviation of the surface potentials $\Phi(\mathbf{r}|\rho^{\mathrm{vac}})$ and $\langle\Phi(\mathbf{r}|\rho_s^{\mathrm{stat}})\rangle_S$ mentioned above. With decreasing complexity of the model R_{DFT} strongly increases measuring 2.7% for TL5P and 5.4% for TL4P. Because of the similarity between the surface potentials $\Phi(\mathbf{r}|\rho^{\mathrm{vac}})$ and $\langle\Phi(\mathbf{r}|\rho_s^{\mathrm{stat}})\rangle_S$, this increase is related to the one observed earlier in Table 1 for the match of the TLνP surface potentials with the DFT/PMM reference.

On the other hand, the quadrupole moments calculated by our DFT approach[8,58−60] (cf. section 2.1) for an isolated water molecule deviate from the experimental data by $R_{\mathrm{DFT}}/\sigma_{\mathrm{exp}} = 3.6\%$ indicating that this DFT method describes the electrostatic signature of an isolated water molecule quite well but not perfectly. This comparison requires the caveat, however, that the experimental liquid phase geometry had been assumed in the DFT calculation, whereas the experimental data pertain to the gas phase geometry. Note in this context that the dipole moment calculated with this DFT approach[43] for an isolated water molecule at the optimized geometry underestimates the experimental gas phase value by 2.4%.

The RMSDs R_{exp} between the quadrupole moments of the various models and the gas phase data (see the last column of Table 3) demonstrate that DFT$^{\mathrm{vac}}$ represents the gas phase data about as well as the TL6P models. Surprisingly also the TL5P model happens to perform well in this respect, whereas for TL4P, in contrast, R_{exp} is by about a factor of 3 larger than for the TL6Ps. For the empirical SWM6 model R_{exp} is even by a factor of about 5 larger despite the fact that, here, the experimental quadrupole moments were among the optimization targets.[65] Note that for the effective model iAMOEBA[39] R_{exp} is similarly large (12%).

3.3. Evaluation. The construction of the two TL6P potentials aimed at water molecules embedded in liquid phase environments at T_0 and $n_{\mathrm{exp}}(T_0,p_0)$. Thus, the quality at which the TL6P liquids resemble water at these conditions are of primary interest and, therefore, we will start with these properties.

Only after a close similarity between liquid water and its computer model at T_0 and p_0 has been demonstrated, issues of transferability gain interest. Examples are the performance at other temperatures,[42] or with respect to the experimentally well-known properties of the isolated water dimer[69−71] and of vapor.[72] Also the TL6P prediction on the melting temperature[73] $T_{\mathrm{exp}}^{\mathrm{m}} = 273.15$ K of ice Ih can add insights here. Correspondingly, these themes will be addressed later in section 4.3.

3.3.1. Targeted Bulk Liquid Properties. Section S7 in the Supporting Information presents and discusses those properties of the liquid at T_0 and $n_{\mathrm{exp}}(T_0,p_0)$, which were targeted during the empirical optimization of the Buckingham parameters A_1, A_2, and B. Here, the $N_iV_iT_0$ test simulations, which were executed for the three system sizes $i \in \{s, m, l\}$, have demonstrated for the two TL6P models that the absolute values of the binding energies $\langle E_{\mathrm{pot}}\rangle$ are by only 0.1−0.4% larger than the target value of −9.92 kcal/mol, that the average pressures $\langle p\rangle$ fluctuate in a small range of ±30 bar around the target value $p_0 = 1$ bar, and that the position r_1 of the first maximum in the RDF $g_{\mathrm{OO}}(r)$ of TL6P is at 2.76 Å as given by Soper's neutron diffraction data[46] whereas r_1 has for TL6P$^{\mathrm{Sk}}$ the required[48] value of 2.80 Å.

3.3.2. Radial Distribution Functions. Interestingly, the RDFs of the two TL6P models, which are depicted in Figure S8 of the Supporting Information, are almost identical for distances larger than 3 Å and match the recent RDF of Skinner et al.[48] very well for distances beyond 4.5 Å. Thus, the differences of the TL6P and TL6P$^{\mathrm{Sk}}$ liquid structures at T_0 are confined to the inner parts of the respective first solvation shells. One might have expected such short ranged differences from the fact that the target r_1 had been coupled to the parameter A_1, which steers the strength of the repulsive part of the Buckingham potential [cf. Equation 1].

3.3.3. Predicted Bulk Liquid Properties. We start the presentation of the TL6P predictions on properties of the liquid water at p_0 and T_0 by shortly sketching the results for the diffusion constant D_0 and viscosity η, for the isothermal compressibility κ_T, and for the isobaric heat capacity C_p. By presenting results on the average dipole moment and on the dielectric constant ϵ_0, we subsequently address in some more detail the important issues of polarity, before we finally turn to the average density $\langle n\rangle$ and its temperature derivative, the thermal expansion coefficient α_p.

Table 4 compares the TL6P predictions enumerated above in the given sequence with corresponding experimental

Table 4. TL6P Bulk Properties Compared with TL5P/TL4P[8] and with Experimental Data

model	$D_0{}^a$	η^b	$\kappa_T{}^c$	$C_p{}^d$	ϵ_0	$\alpha_p{}^e$
TL6P	2.3	0.86	40.1	18.3	77	2.9
TL6P^{Sk}	2.2	0.92	39.7	18.6	79	2.8
TL5P	2.8	0.98	36.4	19.6	67	7.2
TL4P	3.0	0.80	37.4	18.7	77	5.9
exp	2.4[74]	0.81[75]	45.6[26]	18.0[76]	78[27]	2.8[26]

^{a}nm^2/ns. ^{b}mPa s. ^{c}10^{-6}/atm. ^{d}cal/(mol K). ^{e}10^{-4} K^{-1}.

data[26,27,74−76] and with properties[8] of the TL5P and TL4P predecessors (an exception is the density $\langle n \rangle$, which will be separately documented). The statistical errors associated with the TL6P data in Table 4 are listed by Table S10 in section S8.1 of the Supporting Information. Other PMM models are hardly ever mentioned in the following discussion, because extensive and very detailed comparisons of this kind led in ref 8 to the conclusion that TL5P and TL4P feature "bulk phase properties comparable to or even better than those of similarly complex models". Therefore, the TL5P and TL4P descriptions can be safely taken as very good representatives for the large class of similarly complex PMM water models.

3.3.3.1. Self-diffusion Coefficients and Viscosities. Section S8.2 in the Supporting Information explains how the self-diffusion constant D_0 and viscosity η of the infinite system were derived by applying the Dünweg−Kremer formula (eq S12, Supporting Information) to the results of the finite size $N_i V_i T_0$[MI] simulations described in section 2.3. The results of this analysis are collected in the first two data columns and lines of Table 4.

Inspecting the data immediately demonstrates that the two TL6P models describe the experimental diffusivity of liquid water at T_0 and p_0 much better than their predecessors. Instead of considerable overestimates in the range of 17−25%, the more complex TL6P potentials now yield slight underestimates in the range 4−8%. Hence, the TL6P models, whereas approaching the mobility of real water molecules, are considerably less mobile than the TL5P and TL4P models.

A reduced mobility should be concurrently visible in a larger viscosity, which is the case for the TL6P models in comparison with the real liquid but is only partially the case as compared to the earlier models. Compared to TL4P, the TL6P values of η do show the increase expected from the smaller TL6P values for D_0. Compared to TL5P, however, the TL6P values of η are smaller despite the smaller TL6P diffusion constants.

The noted inconsistency is most likely caused by the quite substantial statistical errors of 10−20%, which are according to Table S10 in section S8.1 of the Supporting Information attached to the values of η. These errors are large, because the η-values derive by eq S12 (Supporting Information) from slopes of regression lines, such as those shown by Supporting Information Figure S9 in section S8.2 for the TL6P models, and because the values of such slopes are very sensitive to a small statistical scatter of the underlying data. In contrast, the extrapolated diffusion coefficients show errors of only 1−2% and, hence, are much more reliable.

3.3.3.2. Isothermal Compressibility. A glance at the third data column in Table 4 immediately reveals that also the isothermal compressibility $\kappa_T = (\partial \ln n/\partial p)_T$ at $n_{\exp}$ and T_0 is better described by the TL6P than by the less complex models. The shown model data were derived from the respective $N_s V_{\pm} T_0$ simulations by numerical differentiation.[77] In the

transition from TL4P/TL5P to the TL6P models the underestimates of κ_T are reduced from about 20% to about 12%. Note that according to Table S10 in the Supporting Information the statistical uncertainties $\sigma(\kappa_T)$ are smaller than 1%.

3.3.3.3. Heat Capacity. Additionally including a required quantum correction,[25] the isobaric heat capacity C_p is calculated as a numerical temperature derivative of the total energy per molecule from the $N_s p_0 T_{\pm}$ simulations. The TL6P data on C_p are listed in the fourth data column of Table 4 and feature the same pattern, which we already observed for the diffusivity D_0 and isothermal compressibility κ_T. According to this pattern, TL6P generally performs a little better than TL6P^{Sk} and these two six-point PMM models perform much better than TL5P/TL4P. For $C_p(T_0,p_0)$, in particular, the six-point models thus overestimate the experimental value only by 1−3%, whereas the overestimates provided by the predecessors were larger (4−9%). Because the statistical uncertainties of the C_p values obtained by simulations are in the range of 2% (cf. Supporting Information Table S10), the heat capacity predicted by TL6P, in particular, is statistically indistinguishable from the experimental value.

3.3.3.4. Dipole Distributions. Section S8.3 in the Supporting Information presents and discusses the PMM dipole distributions resulting from the $N_m V_m T_0$ simulations of the TL6P models. The resulting average dipole moments $\langle \mu \rangle$ are almost equal at about 2.53 D.

With this value the average dipole moments $\langle \mu \rangle$ are very close to the averages $\langle \mu_{DFT/PMM} \rangle \approx 2.54$ D of the DFT/PMM dipole moments, which were employed to optimize the Gaussian widths σ of the inducible TL6P dipoles (cf. section S2 in the Supporting Information). Thus, the TL6P potentials not only represent the static part $\langle \Phi(\mathbf{r}|\rho_s^{stat}) \rangle_S$ of the DFT/PMM mean field surface potential very well (cf. section 3.1) but also excellently mimic the dipolar response properties of their DFT/PMM prototypes.

Furthermore, the TL6P averages $\langle \mu \rangle$ are in the range 2.4−2.6 D. It has been previously suggested that only those PMM models can have a dielectric constant ϵ close to the experimental value $\epsilon(T_0,p_0)$, whose average dipole moments $\langle \mu \rangle$ are in the given range.[29,78] Thus one may expect that the dielectric constants of the two TL6P potentials match $\epsilon(T_0,p_0)$ quite well.

3.3.3.5. Dielectric Constant. In computations of the dielectric constant ϵ special care has to be taken, if one employs, like our MD program IPHIGENIE,[51] a moving-boundary reaction field approach[55] for the treatment of the long-range electrostatics. In this computational scenario, the simulated system is enclosed by toroidal boundary conditions[9] and is, beyond the distance dictated by the minimum image convention,[9] embedded in a dielectric continuum with the dielectric constant ϵ_{RF}. If the dielectric constant ϵ of the simulated model differs from ϵ_{RF}, then the value calculated for ϵ by Neumann's[79] formula (cf. eq 8 in ref 8) from the fluctuations of the total dipole moment in a $N_i V_i T_0$ simulation depends on V_i. This size dependence can be diminished by applying an iterative correction,[80] which is based on perturbation theory. But nevertheless, the finite size results $\epsilon(N_i V_i T_0)$ must be eventually extrapolated to the value ϵ_0 applicable to the infinitely large system.

The data resulting from the $N_i V_i T_0$ simulations [i ∈ {s, m, l}] are represented in Figure 3 as functions of the inverse box lengths L^{-1} together with regression lines, which enable
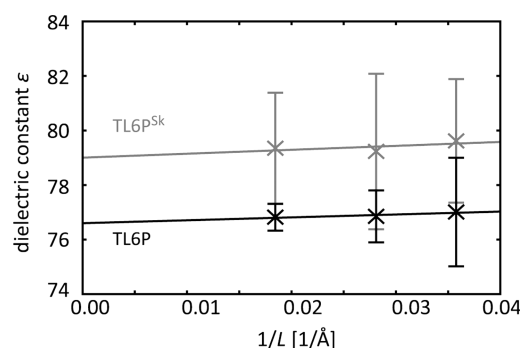
Figure 3. Size dependent dielectric constants $\epsilon(N_iV_iT_0)$ calculated for TL6P (black crosses) and TL6P^{Sk} (gray crosses) together with error bars indicating statistical uncertainties, which were calculated as described in the text. The depicted linear regressions serve to extrapolate to the respective dielectric constants ϵ_0 of the infinite systems at $L^{-1} = 0$.

extrapolations to the infinite systems at $L^{-1} = 0$. The linear regressions assign errors $\sigma(\epsilon_0)$ to the extrapolated values ϵ_0, which are smaller than 1% (cf. Table S10 in the Supporting Information). To estimate the statistical errors of the simulation results $\epsilon(N_iV_iT_0)$, the associated trajectories were partitioned into two parts. The deviations of the two values $\epsilon_k(N_iV_iT_0)$, = 1, 2, from their common average were taken as measures for the associated standard deviations and are drawn as error bars in Figure 3.

In agreement with the above expectations, which were based on the TL6P values of the average dipole moments $\langle\mu\rangle$, the extrapolated dielectric constants ϵ_0 deviate from the experimental value by only about 1%. A similarly close value had been previously obtained for TL4P, whereas the dielectric constant of TL5P showed a much larger (14%) deviation (Table 4).

In the Introduction we have pointed out that PMM models, whose electrostatic signatures are described by three or four charges at fixed positions within the molecule, cannot concomitantly describe the dielectric constant ϵ and the thermal expansion coefficient α_p at p_0 and T_0 with a comparable accuracy. Having ascertained that the TL6P models reproduce ϵ very well at these conditions, we now turn to their performances on the average density $\langle n\rangle$ and its temperature derivative α_p.

3.3.3.6. Average Density at p_0. As is documented by Table S12 in section S8.4 of the Supporting Information, the $N_ip_0T_0$ simulations predict for both TL6P models average densities $\langle n_i\rangle(T_0,p_0)$ that agree, independently of the system size i ∈ {s, m, l}, remarkably well with the experimental value[26] of 0.9965 g/cm³. The deviations of the simulated values $\langle n_i\rangle(T_0,p_0)$ from the experimental one are smaller than the largest statistical error of the simulation data, which is 0.3%.

3.3.3.7. Thermal Expansion Coefficient. The isobaric thermal expansion coefficients were approximately calculated from the $N_sp_0T_\pm$ simulations according to[81]

$$\alpha_p \approx -\frac{\ln[\langle n\rangle(p_0,T_+)] - \ln[\langle n\rangle(p_0,T_-)]}{T_+ - T_-} \tag{11}$$

by numerical differentiation with $T_\pm = T_0 \pm 10$ K.

Surprisingly, the resulting values, which are listed in Table 4, match the experimental reference extremely well for both TL6P models showing deviations of at most 4%. Note that these

descriptions of α_p are even better than the ones achieved by those previous models (TIP4P/2005[40] and BKd3[34]), which performed exceptionally well ($\approx\pm10\%$) on this particular observable, because α_p had been among the targets of the respective empirical optimization. Within the statistical uncertainties $\sigma(\alpha_p) = 0.6 \times 10^{-4}$ K^{-1} given in Table S10 of the Supporting Information, the two TL6P simulation results for α_p are indistinguishable from the experimental value.

The electrostatically less complex predecessor models, in contrast, show overestimates by factors of 2.1−2.6. When TL6P is compared to TL5P, it is the addition of a negative charge q_M = −0.57 e on the bisectrix of the HOH triangle at the quite large distance l_{OM} = 0.38 Å together with slightly modified positions and values of the "lone pair" charges q_L (cf. Table 2) that apparently causes the substantially improved description of the isobaric thermal expansion coefficient $\alpha_p(T_0,p_0)$.

Concerning α_p, the details of the electrostatic signatures of the TL6P models are of key importance as one can see by reconsidering Figure 2, which compares the electrostatic geometry of TL6P with that of the empirically parametrized[65] seven-point PMM model SWM6. Whereas SWM6 reproduces, just like TL6P, the dielectric constant $\epsilon(T_0,p_0)$ very well, it overestimates, just like TL5P and in contrast to TL6P, α_p by a factor of about 2.6 (we have extracted the SWM6 value $\alpha_p \approx$ 7.2 $\times$ 10^{-4} K^{-1} from the temperature dependence of the density depicted in Figure 5 of ref 65).

4. DISCUSSION

With the mixed computational and empirical optimization of the six-point potentials TL6P and TL6P^{Sk} we finally succeeded with the construction of excellent PMM models for liquid water at T_0 and p_0. The TL6P potentials reproduce, of course, all those liquid phase properties that were targeted by the empirical optimization of the Buckingham potential employed for the modeling of the van der Waals interactions. Beyond that, they accurately predict a series of liquid phase properties, i.e., the self-diffusion constant D_0, viscosity η, isothermal compressibility κ_T, isobaric heat capacity C_p, and dielectric constant ϵ, for which also other PMM models with a related design typically yield reasonable descriptions. But finally and most remarkably they even provide accurate descriptions of the isobaric thermal expansion coefficient α_p, for which PMM models tend to fail.

4.1. Electrostatic Signatures. Moreover, the method of parameter optimization employed by us, which derives the electrostatic signatures of water models almost exclusively from DFT/PMM hybrid calculations, has eventually revealed the microscopic physical reason, why previous PMM models failed in accurately predicting $\alpha_p(T_0,p_0)$. According to the analysis of the quality, by which TL6P and its TL5P and TL4P predecessors can represent the average electrostatic signature of the DFT/PMM reference models (cf. the second line in Table 1 in section 3.1), it is the prominent feature of the TL6P potentials that they reproduce the average static part of the surface potential of a DFT water model embedded in a PMM liquid phase environment substantially better than than TL5P and TL4P and almost as good as an isolated DFT model of the same liquid phase geometry. The latter fact that the isolated DFT model excellently approximates the average static part of the surface potential of a DFT model in a PMM liquid (cf. section 3.1) furthermore explains why the TL6P quadrupole moments are much closer to those of an isolated DFT water molecule than TL5P or TL4P and as close to the experimental

gas phase data[69] as the DFT result for an isolated molecule (cf. Table 3).

Thus, the electrostatic signatures of TL5P, TL4P, SWM6, and related models do not describe the almost constant higher electrostatic moments (quadrupole, octupole, hexadecapole, ...) of liquid phase water molecules with sufficient accuracy. In contrast, DFT and DFT/PMM descriptions and the correspondingly optimized TL6P potentials can cover these higher moments with errors of at most 3% (cf. Tables 1 and 3).

Because the electrostatic fields generated by the higher electrostatic moments are increasingly short ranged, they predominantly shape the local liquid structure in the immediate neighborhood of a given water molecule. Apparently, only models like TL6P, which reproduce the local fields generated by liquid phase water molecules very well, do not grossly overestimate the very small density reduction, which is induced by a temperature decrease near T_0 and is expressed by the small value of $\alpha_p(T_0,p_0)$.

It should be stressed that the high quality, by which DFT and DFT/PMM descriptions can cover the properties of water molecules in the liquid, lies at the heart of the apparent success of the PMM model construction reached with the TL6P potentials. Together with adopting the experimental gas phase values μ_{exp}^g and α_{exp}^g for the static dipole moment and the polarizability of the model, it was the separate DFT/PMM optimization of the width σ of the Gaussian inducible dipole at the oxygen and of the constant electrostatic signature $\Lambda_{e,6}$ that reduced the parameter space to a sufficiently low dimension such that the unusual electrostatic TL6P geometry depicted in Figure 1 could be determined.

4.2. van der Waals Potentials. In contrast to the electrostatic properties, the empirically optimized Buckingham parameters turned out to be in a range in which also previous potentials can be found. As compared to the cases for TL5P and TL4P, the dispersion attraction of the two TL6P models, for instance, turned out to be reduced by about a factor of 2, moving it close to the dispersion attraction of the well-known nonpolarizable TIP5P and TIP4P/2005 models.[40,82] On the other hand, the resulting differences between the Buckingham potentials of the two TL6P models were quite small despite the fact that different experimental targets[46,48] were used for the optimization of A_1 (cf. Figure S8 of the Supporting Information). In view of the slightly superior performance of TL6P as compared to TL6P^{Sk} concerning most observables [with the exception of $\alpha_p(T_0,p_0)$, cf. Table 4], we decided to consider the latter TL6P variant not any further.

4.3. Transferability Issues. As mentioned above at several locations, the TL6P potential turned out[42] to predict the temperature density profile $n_{exp}(T,p_0)$ of liquid water for $T \in$ [250, 320] K with an unprecedented accuracy as expressed by a root-mean square density deviation of only 0.0005 g/cm³. In line with the small 0.1×10^{-4} K^{-1} overestimate of $\alpha_p(T_0,p_0)$ by TL6P, this deviation is a likewise small density overestimate, which increases for decreasing temperatures $T < T_0$.

For PMM water models with an inducible dipole and otherwise static partial point charges like TL6P, an overestimated density of the supercooled liquid indicates that the structure forming local electrostatic interactions, which are due to the higher electrostatic multipole moments and reduce the density,[42] do not sufficiently compete with the general attractive forces, which are caused by the dipolar and dispersive interactions. Correspondingly, one expects that such a model underestimates the stability of ice and overestimates that of the

liquid entailing an underestimate of the melting temperature T^m (see further below).

Because TL6P^{Sk} performs on the temperature derivative $\alpha_p(T_0,p_0)$ of the density even better than TL6P, it might have been preferential to use this variant model potential in the computationally very costly 20 ns RE-MD simulations[42] on $n_{exp}(T,p_0)$. The answer to the question, however, to what extent the excellent performance of TL6P on $n_{exp}(T,p_0)$ can be further optimized by minor parameter variations must be left to future studies. In the case of TL6P, the observed[26] temperature $T_{exp}^{md} = $ 277.134 K of maximum density was hit by the prediction T_{TL6P}^{md} = 277.055 ± 0.125 K within the limits of a very small statistical uncertainty.[42]

As compared to these structural properties, the TL6P predictions on the temperature profiles of energetic liquid phase properties like the heat of vaporization $\Delta H_{vap}(T,p_0)$ or the heat capacity $C_p(T,p_0)$ turned out to be a little worse.[42] Both quantities showed small but, toward lower temperatures, increasing overestimates of the corresponding experimental findings. As a possible cause the use of partial point charges instead of Gaussian charges (with their locally slightly softer electrostatic potentials) was identified (see the Supporting Information to ref 42).

4.3.1. Melting Temperature. In section S10 of the Supporting Information we have presented and applied a simulation setup for mixtures of ice Ih and liquid water. The setup was designed to measure the average potential energies $E_{pot}(t|T_z)$ of the water molecules as a function of the time t in Np_0T_z simulations covering N = 4424 water molecules at a series of temperatures T_z near the melting temperature T_{model}^m of the respective PMM or MM model. Measuring the temporal slope of $E(t|T_z)$ as a function of temperature, we determined the prediction T_{model}^m as the temperature of vanishing slope.

The simulation setup has been tested using the well-known nonpolarizable model TIP4P/2005 as a reference, which predicts[40,83] a melting temperature of about 250 ± 3 K. Our setup yielded the value $T_{TIP4P/2005}^m$ = 247.5 K, demonstrating that it gives a reasonable estimate and lower bound. In line with the fact that the TL4P predecessor model strongly overestimates[42] the liquid's density $n_{exp}(T_{exp}^m,p_0)$ by 0.96% at the experimental melting temperature[73] T_{exp}^m = 273.15 K, our setup locates its melting temperature T_{TL4P}^m way below 250 K, which was the lowest temperature that could be reasonably treated by our PMM setup. This result is similar to that of the related PMM four-point model SWM4/NDP,[31] which overestimates $n_{exp}(T_{exp}^m,p_0)$ by as much as 1.32% and underestimates[84] T_{exp}^m by 88 K.

In contrast, and as expected from the very small 0.02% overestimate of $n_{exp}(T_{exp}^m,p_0)$ by TL6P, this PMM model predicts T_{TL6P}^m = 262.5 K, thus underestimating T_{exp}^m by at most 11 K. As shown in section S10 of the Supporting Information, the TL6P model apparently predicts T_{exp}^m more accurately than any other PMM model known to us.

4.3.2. Vapor. Applying a novel DFT/PMM technology,[14] the electrostatics of the TLνP models was optimized for liquid phase environments at T_0 and p_0. Therefore, one expects a suboptimal performance on gas phase properties. As an illustration, we compute in section S4 of the Supporting Information the second virial coefficients $B_2(T)$ of the TLνP models (ν = 4, 5, 6) for $T \in$ [300, 450]. The results are compared with those of other models (including a variant PMM six-point model called TL6P^g, which has been tentatively

optimized by DFT calculations for the gas phase) and with experimental data.[72]

On average, the TL6P predictions on the absolute values $|B_2(T)|$ turned out to be by 9% smaller than the experimental values, TL4P showed underestimates of only 3%, whereas the "gas phase" model TL6P^g was very close to the experimental data closely resembling the behavior of the BK3 model.[36] As expected, TL6P is definitely not an optimal model for water vapor.

4.3.3. Isolated Dimer. Scrutinizing the performance in further environments we present and discuss in section S5 of the Supporting Information the geometries $\mathbf{G}_d$, binding energies $E_{\text{pot,d}}$, and total dipole moments μ_d of the isolated TL6P dimers. Here it is shown that the two TL6P models generally furnish reasonable descriptions, which are of quality similar to those provided by their less complex predecessors[8] but cannot compete, e.g., with SWM6, because dimer properties had been optimization targets in this case.[65]

4.3.4. DFT/PMM Settings. As opposed to descriptions of the gas phase, the TL6P water model should be excellently suited for DFT/PMM-MD simulations of solute−solvent systems, which aim, by choosing the solute as the DFT fragment, at the accurate calculation of its condensed phase infrared spectrum (see, e.g., refs 85 and 86 for less accurate DFT/MM-MD examples, which were severely hampered[87] by the low quality of the respective MM solvent model). The high quality, by which the TL6P/DFT and DFT/TL6P dimers could reproduce corresponding experimental data (cf. section S6 and Table S8 in the Supporting Information) are a first indication for the favorable properties of TL6P in DFT/PMM settings. A second indication is the near identity of the TL6P liquid phase dipole distribution with the one calculated for a liquid phase DFT/TL6P ensemble (cf. section 3.3.3 and Supporting Information S8.3).

4.4. Computational Aspects. Issues of computational manageability are discussed in some detail in section S9 of the Supporting Information. Comparing MD simulations of systems comprising either 1500 polarizable TL3P or non-polarizable TIP3P models,[88] one sees that the computer time spent by our PMM-MD program IPHIGENIE[51] increases by a factor of 3.5 upon adding an inducible Gaussian dipole, whose self-consistency iterations have to be brought to convergence. The transition to TL4P implies another factor of 1.3, which then marks the minimum effort required for a reasonably accurate description. A comparatively small factor of about 1.15 eventually characterizes the transition from TL4P to TL6P.

Interestingly, this increase of computer time is almost identical to the time that has to be spent on exchanging the three partial point charges of TL4P by Gaussian charge distributions. The thus obtained model then resembles GCPM[30] and the various[34,36,64,89] BK models. In summary, replacing TL4P by TL6P implies only a small computational overhead while yielding a significant accuracy gain. Compared to the simplistic TIP3P model, the computer time consumed by TL6P is 5.2 times larger, which is, however, compensated by an enormous gain of accuracy.

5. SUMMARY AND OUTLOOK

The mixed computational and empirical approach to the optimization of PMM models for complex liquids such as water, which has been developed in ref 8, relies on a novel DFT/PMM technology[14] and led to the suggestion of the quite reasonable PMM four- and five-point water models TL4P and

TL5P, respectively, has now been successfully applied to the development of two corresponding six-point PMM models. The parametrization and a series of test simulations were executed at the single point $T_0 = 300$ K and $p_0 = 1$ bar of the thermodynamic state space. Here, the TL6P and TL6P^{Sk} potentials showed a remarkably good performance, which could be identified to follow from their closely resembling but unusual electrostatic signatures.

In particular, the TL6P potentials were shown to accurately predict a series of important liquid phase properties. These properties were, of course, not among the three experimental targets employed for the empirical optimization, which served to tune solely the three van der Waals parameters (A_1, A_2 B). Among the predicted properties were the dielectric constant $\epsilon(T_0,p_0)$, the density, and its negative temperature derivative, the isobaric thermal expansion coefficient $\alpha_p(T_0,p_0)$, of liquid water.

The latter finding had nourished the hope that one of the TL6P potentials might also correctly predict the density $n(T,p_0)$ over a sufficiently wide range of other temperatures, which extends beyond the temperature $T^{\text{md}} = 277$ K of maximum density to lower values. Therefore, this issue has been addressed in a thorough follow-up study,[42] which applied 20 ns RE-MD simulations spanning the temperature range [250, 320] K to the TLνP models with $\nu = 4, 5, 6$. In line with the quite accurate value of $\alpha_p(T_0,p_0)$ also the density profile $n(T,p_0)$ and the temperature T^{md} of maximum density were predicted by TL6P with a hitherto unprecedented accuracy (as compared to TL4P, TL5P, and other PMM models).

This success of TL6P and the corresponding failure of its less complex predecessors TL4P and TL5P, which had been parametrized by the same procedure, led to the conclusion[42] that the TL6P distribution of partial point charges depicted in Figure 2 provides a minimal cartoon for those aspects of the continuous charge distributions in real water molecules, which are responsible for the density anomaly.

In line with the very slight (0.02%) overestimate of the density at the experimental melting temperature T^m_{exp}, TL6P underestimates this temperature only a little by at most 11 deg. As is shown in section S10 of the Supporting Information, no other PMM water model known to us performs with a comparable accuracy in predicting T^m_{exp}. The predecessor model TL4P, in particular, assigns the melting point of ice to temperatures way below 250 K. This finding strengthens the conclusions of ref 42 concerning the enormous jump of modeling accuracy, which can be achieved in a DFT/PMM parametrization setting through the transition from four- and five- to six-point PMM models.

The polarizable six-point model TL6P, which was successfully developed in this contribution by applying DFT/PMM hybrid techniques, does not represent a final word but should be understood, instead, as a new beginning. Here, one first should check whether and, if so, to what extent the variant model TL6P^{Sk}, which was also described above, can further reduce the already small TL6P overestimate of $n_{\text{exp}}(T,p_0)$ at temperatures $T < T_0$ and the small TL6P underestimate of the melting temperature T^m_{exp}

Next, the influence of the DFT functional, which is employed in the DFT/PMM parametrization procedure, on the resulting bulk phase properties should be studied. We employed, for reasons of reduced computational cost, the rather simple gradient-corrected Becke−Perdew functional.[58,59] Including Hartree−Fock exchange[90] into the popular Becke−Lee−

Yang–Parr approach,[58,91] that is, using the so-called B3LYP functional promises more accurate descriptions (see, e.g., ref 87). Hence, six-point PMM models of the TL6P-type should be calculated by the B3LYP/PMM technique and evaluated. All these six-point PMM models will have the same computational complexity as TL6P.

Finally, and at the expense of an enhanced computational cost, one could try to construct PMM six-point models, in which the five static partial point charges are modeled as Gaussian distributions. This should be done if (and only if) the thus far constructed PMM six-point models still feature at low temperatures a somewhat overestimated heat of vaporization.

■ ASSOCIATED CONTENT

ⓢ Supporting Information

The Supporting Information provides on 27 pages in ten sections a total of nine figures (S4–S12), eight tables (S5–S12), and various pieces of text explaining and documenting several issues. First we specify the computation of the long-range electrostatics in some detail, and then we sketch the correlations between DFT/PMM and PMM dipoles, which are used for the optimization of the widths of the Gaussian inducible dipoles. Next we give the parameters of the two TL6P models with all relevant digits. After a discussion of the second virial coefficient and the PMM and DFT/PMM dimer properties, we study all those properties, which were targets of the empirical optimization. Furthermore, we provide TL6P predictions on bulk phase properties and associated statistical errors. After discussing computational issues, we finally describe MD simulations on mixtures of ice Ih and liquid water. This material is available free of charge via the Internet at http://pubs.acs.org/.

■ AUTHOR INFORMATION

Corresponding Author

*P. Tavan: e-mail, tavan@physik.uni-muenchen.de.

Notes

The authors declare no competing financial interest.

■ ACKNOWLEDGMENTS

■ REFERENCES

(1) Ball, P. *H₂O: A Biography of Water*; Phoenix, Orion Books Ltd: London, U.K., 2000.

(2) Guillot, B. A Reappraisal of What We Have Learnt During Three Decades of Computer Simulations on Water. *J. Mol. Liq.* **2002**, *101*, 219–260.

(3) Lopes, P.; Roux, B.; MacKerell, A. Molecular Modeling and Dynamics Studies with Explicit Inclusion of Electronic Polarizability: Theory and Applications. *Theor. Chem. Acc.* **2009**, *124*, 11–28.

(4) Dünweg, B.; Kremer, K. Molecular Dynamics Simulation of a Polymer Chain in Solution. *J. Chem. Phys.* **1993**, *99*, 6983–6997.

(5) Salacuse, J. J.; Denton, A. R.; Egelstaff, P. A. Finite-Size Effects in Molecular Dynamics Simulations: Static Structure Factor and Compressibility. I. Theoretical Method. *Phys. Rev. E* **1996**, *53*, 2382–2389.

(6) Rapaport, D. C. *The Art of Molecular Dynamics Simulation*; Cambridge University Press: Cambridge, U.K., 2004.

(7) Tazi, S.; Botan, A.; Salanne, M.; Marry, V.; Turq, P.; Rotenberg, B. Diffusion Coefficient and Shear Viscosity of Rigid Water Models. *J. Phys.: Condens. Matter* **2012**, *24*, 284117.

(8) Tröster, P.; Lorenzen, K.; Schwörer, M.; Tavan, P. Polarizable Water Models from Mixed Computational and Empirical Optimization. *J. Phys. Chem. B* **2013**, *117*, 9486–9500.

(9) Allen, M. P.; Tildesley, D. *Computer Simulations of Liquids*; Clarendon: Oxford, U.K., 1987.

(10) Vega, C.; Abascal, J. Simulating Water with Rigid Non-Polarizable Models: A General Perspective. *Phys. Chem. Chem. Phys.* **2011**, *13*, 19663–19688.

(11) Guidon, M.; Hutter, J.; VandeVondele, J. Robust Periodic Hartree-Fock Exchange for Large-Scale Simulations Using Gaussian Basis Sets. *J. Chem. Theory Comput.* **2009**, *5*, 3010–3021.

(12) Guidon, M.; Hutter, J.; VandeVondele, J. Auxiliary Density Matrix Methods for Hartree-Fock Exchange Calculations. *J. Chem. Theory Comput.* **2010**, *6*, 2348–2364.

(13) Tavan, P.; Carstens, H.; Mathias, G. Molecular Dynamics Simulations of Proteins and Peptides: Problems, Achievements, and Perspectives. In *Protein Folding Handbook*; Buchner, J., Kiefhaber, T., Eds.; Wiley-VCH: Weinheim, 2005; Vol. 1, pp 1170–1195.

(14) Schwörer, M.; Breitenfeld, B.; Tröster, P.; Lorenzen, K.; Tavan, P.; Mathias, G. Coupling DFT to Polarizable Force Fields for Efficient and Accurate Hamiltonian Molecular Dynamics Simulations. *J. Chem. Phys.* **2013**, *138*, 244103.

(15) The letters "TL" in the names TLvP of or water models are the initials of the first two authors of ref 8 the number $v \in \{3, 4, 5, 6\}$ counts the points of force action within the respective model, and "P" stands for "point".

(16) Clough, S.; Beers, Y.; Klein, G.; Rothman, L. Dipole Moment of Water from Stark Measurements of H₂O, HDO, and D₂O. *J. Chem. Phys.* **1973**, *59*, 2254–2259.

(17) Murphy, W. F. The Rayleigh Depolarization Ratio and Rotational Raman Spectrum of Water Vapor and the Polarizability Components for the Water Molecule. *J. Chem. Phys.* **1977**, *67*, 5877–5882.

(18) Buckingham, R. A.; Corner, J. Tables of Second Virial and Low-Pressure Joule-Thomson Coefficients for Intermolecular Potentials with Exponential Repulsion. *Proc. R. Soc. London, Ser. A* **1947**, *189*, 118–129.

(19) Ichikawa, K.; Kameda, Y.; Yamaguchi, T.; Wakita, H.; Misawa, M. Neutron-Diffraction Investigation of the Intramolecular Structure of a Water Molecule in the Liquid Phase at High Temperatures. *Mol. Phys.* **1991**, *73*, 79–86.

(20) Thiessen, W. E.; Narten, A. H. Neutron Diffraction Study of Light and Heavy Water Mixtures at 25 °C. *J. Chem. Phys.* **1982**, *77*, 2656–2662.

(21) Wallqvist, A.; Berne, B. Effective Potentials for Liquid Water Using Polarizable and Nonpolarizable Models. *J. Phys. Chem.* **1993**, *97*, 13841–13851.

(22) de Pablo, J. J.; Prausnitz, J. M.; Strauch, H. J.; Cummings, P. T. Molecular Simulation of Water along the Liquid–Vapor Coexistence Curve from 25°C to the Critical Point. *J. Chem. Phys.* **1990**, *93*, 7355–7359.

(23) Kiyohara, K.; Gubbins, K. E.; Panagiotopoulos, A. Z. Phase Coexistence Properties of Polarizable Water Models. *Mol. Phys.* **1998**, *94*, 803–808.

(24) Straatsma, T. P.; McCammon, J. A. Molecular Dynamics Simulations with Interaction Potentials Including Polarization Development of a Noniterative Method and Application to Water. *Mol. Simul.* **1990**, *5*, 181–192.

(25) Yu, H.; Hansson, T.; Van Gunsteren, W. Development of a Simple, Self-Consistent Polarizable Model for Liquid Water. *J. Chem. Phys.* **2003**, *118*, 221–234.

(26) Kell, G. Precise Representation of Volume Properties of Water at One Atmosphere. *J. Chem. Eng. Data* **1967**, *12*, 66–69.

(27) Kaatze, U. Complex Permittivity of Water as a Function of Frequency and Temperature. *J. Chem. Eng. Data* **1989**, *34*, 371–374.

(28) Yu, H.; van Gunsteren, W. Charge-On-Spring Polarizable Water Models Revisited: From Water Clusters to Liquid Water to Ice. *J. Chem. Phys.* **2004**, *121*, 9549–9564.

(29) Lamoureux, G.; MacKerell, A., Jr.; Roux, B. A Simple Polarizable Model of Water Based on Classical Drude Oscillators. *J. Chem. Phys.* **2003**, *119*, 5185−5197.

(30) Paricaud, P.; Předota, M.; Chialvo, A.; Cummings, P. From Dimer to Condensed Phases at Extreme Conditions: Accurate Predictions of the Properties of Water by a Gaussian Charge Polarizable Model. *J. Chem. Phys.* **2005**, *122*, 244511.

(31) Lamoureux, G.; Harder, E.; Vorobyov, I.; Roux, B.; MacKerell, A. A Polarizable Model of Water for Molecular Dynamics Simulations of Biomolecules. *Chem. Phys. Lett.* **2006**, *418*, 245−249.

(32) Kunz, A.; van Gunsteren, W. Development of a Nonlinear Classical Polarization Model for Liquid Water and Aqueous Solutions: COS/D. *J. Phys. Chem. A* **2009**, *113*, 11570−11579.

(33) Viererblová, L.; Kolafa, J. A Classical Polarizable Model for Simulations of Water and Ice. *Phys. Chem. Chem. Phys.* **2011**, *13*, 19925−19935.

(34) Kiss, P. T.; Baranyai, A. Density Maximum and Polarizable Models of Water. *J. Chem. Phys.* **2012**, *137*, 084506.

(35) Lennard-Jones, J. E. Cohesion. *Proc. Phys. Soc.* **1931**, *43*, 461−482.

(36) Kiss, P. T.; Baranyai, A. A Systematic Development of a Polarizable Potential of Water. *J. Chem. Phys.* **2013**, *138*, 204507.

(37) Data extracted at T_0 from Figure 8 in ref 36.

(38) Effective mean-field type potentials, which try to compensate the fully (e.g., TP4P/2005[40]) or partially (e.g., iAMOEBA[39]) neglected polarizability by an empirically optimal but nevertheless nonphysical choice of the model parameters, may be of practical use in simulations but are almost certainly of limited value for predictions on conditions, which are not covered by the reference data (e.g., water in proteins, electrolytes, etc.). PMM models, in contrast, which are good enough to catch the essential physics of a water molecule, should be transferable to all kinds of environments as long as the assumption of linear response is valid. Furthermore they open the chance to identify the microscopic causes for the macroscopic properties of water.

(39) Wang, L.-P.; Head-Gordon, T.; Ponder, J. W.; Ren, P.; Chodera, J. D.; Eastman, P. K.; Martinez, T. J.; Pande, V. S. Systematic Improvement of a Classical Molecular Model of Water. *J. Phys. Chem. B* **2013**, *117*, 9956−9972.

(40) Abascal, J.; Vega, C. A General Purpose Model for the Condensed Phases of Water: TIP4P/2005. *J. Chem. Phys.* **2005**, *123*, 234505.

(41) Alejandre, J.; Chapela, G. A.; Saint-Martin, H.; Mendoza, N. A Non-Polarizable Model of Water that Yields the Dielectric Constant and the Density Anomalies of the Liquid: TIP4Q. *Phys. Chem. Chem. Phys.* **2011**, *13*, 19728−19740.

(42) Tröster, P.; Tavan, P. The Microscopic Physical Cause for the Density Maximum of Liquid Water. *J. Phys. Chem. Lett.* **2014**, *5*, 138−142.

(43) Schropp, B.; Tavan, P. Flexibility Does Not Change the Polarizability of Water Molecules in the Liquid. *J. Phys. Chem. B* **2010**, *114*, 2051−2057.

(44) Berweger, C.; van Gunsteren, W.; Müller-Plathe, F. Force Field Parametrization by Weak Coupling. Re-Engineering SPC Water. *Chem. Phys. Lett.* **1995**, *232*, 429−436.

(45) Hura, G.; Sorenson, J.; Glaeser, R.; Head-Gordon, T. A High-Quality X-Ray Scattering Experiment on Liquid Water at Ambient Conditions. *J. Chem. Phys.* **2000**, *113*, 9140−9148.

(46) Soper, A. K. The Radial Distribution Functions of Water and Ice from 220 to 673 K and at Pressures up to 400 MPa. *Chem. Phys.* **2000**, *258*, 121−137.

(47) Soper, A. K. Joint Structure Refinement of X-Ray and Neutron Diffraction Data on Disordered Materials: Application to Liquid Water. *J. Phys.: Condens. Matter* **2007**, *19*, 335206.

(48) Skinner, L. B.; Huang, C.; Schlesinger, D.; Pettersson, L. G.; Nilsson, A.; Benmore, C. J. Benchmark Oxygen-Oxygen Pair-Distribution Function of Ambient Water from X-Ray Diffraction Measurements with a Wide Q-Range. *J. Chem. Phys.* **2013**, *138*, 074506.

(49) Jancso, G.; Van Hook, W. A. Condensed Phase Isotope Effects. *Chem. Rev.* **1974**, *74*, 689−750.

(50) Wagner, W.; Pruß, A. The IAPWS Formulation 1995 for the Thermodynamic Properties of Ordinary Water Substance for General and Scientific Use. *J. Phys. Chem. Ref. Data* **2002**, *31*, 387.

(51) Lorenzen, K.; Schwörer, M.; Tröster, P.; Mates, S.; Tavan, P. Optimizing the Accuracy and Efficiency of Fast Hierarchical Multipole Expansions for MD Simulations. *J. Chem. Theory Comput.* **2012**, *8*, 3628−3636.

(52) Niedermeier, C.; Tavan, P. A Structure Adapted Multipole Method for Electrostatic Interactions in Protein Dynamics. *J. Chem. Phys.* **1994**, *101*, 734−748.

(53) Niedermeier, C.; Tavan, P. Fast Version of the Structure Adapted Multipole Method: Efficient Calculation of Electrostatic Forces in Protein Dynamics. *Mol. Simul.* **1996**, *17*, 57−66.

(54) Eichinger, M.; Grubmüller, H.; Heller, H.; Tavan, P. FAMUSAMM: An Algorithm for Rapid Evaluation of Electrostatic Interactions in Molecular Dynamics Simulations. *J. Comput. Chem.* **1997**, *18*, 1729−1749.

(55) Mathias, G.; Egwolf, B.; Nonella, M.; Tavan, P. A Fast Multipole Method Combined with a Reaction Field for Long-Range Electrostatics in Molecular Dynamics Simulations: The Effects of Truncation on the Properties of Water. *J. Chem. Phys.* **2003**, *118*, 10847−10860.

(56) Eichinger, M.; Tavan, P.; Hutter, J.; Parrinello, M. A Hybrid Method for Solutes in Complex Solvents: Density Functional Theory Combined with Empirical Force Fields. *J. Chem. Phys.* **1999**, *110*, 10452−10467.

(57) CPMD V3.9, Copyright IBM Corp 1990−2008, Copyright MPI für Festkörperforschung Stuttgart 1997-2001, see also www.cpmd.org.

(58) Becke, A. D. Density-Functional Exchange-Energy Approximation with Correct Asymptotic Behavior. *Phys. Rev. A* **1988**, *38*, 3098−3100.

(59) Perdew, J. P. Density-Functional Approximation for the Correlation Energy of the Inhomogeneous Electron Gas. *Phys. Rev. B* **1986**, *33*, 8822−8824.

(60) Troullier, N.; Martins, J. Efficient Pseudopotentials for Plane-Wave Calculations. *Phys. Rev. B* **1991**, *43*, 1993−2006.

(61) Bussi, G.; Parrinello, M. Stochastic Thermostats: Comparison of Local and Global Schemes. *Comput. Phys. Commun.* **2008**, *179*, 26−29.

(62) Lingenheil, M.; Denschlag, R.; Reichold, R.; Tavan, P. The Hot-Solvent/Cold-Solute Problem Revisited. *J. Chem. Theory Comput.* **2008**, *4*, 1293−1306.

(63) Berendsen, H. J. C.; Postma, J. P. M.; van Gunsteren, W. F.; DiNola, A.; Haak, J. R. Molecular Dynamics with Coupling to an External Bath. *J. Chem. Phys.* **1984**, *81*, 3684−3690.

(64) Baranyai, A.; Kiss, P. A Transferable Classical Potential for the Water Molecule. *J. Chem. Phys.* **2010**, *133*, 144109.

(65) Yu, W.; Lopes, P. E. M.; Roux, B.; MacKerell, A. D.; Six-Site, J. Polarizable Model of Water Based on the Classical Drude Oscillator. *J. Chem. Phys.* **2013**, *138*, 034508.

(66) Nada, H.; van der Eerden, J. An Intermolecular Potential Model for the Simulation of Ice and Water Near the Melting Point: A Six-Site Model of H_2O. *J. Chem. Phys.* **2003**, *118*, 7401−7413.

(67) The electrostatic signature of the early nonpolarizable six-point model suggested in ref 66 strongly differs from that of TL6P, because it is an effective[38] potential. For instance, the angle φ_{LOL} between the very small lone-pair charges (-0.044 e) is $111°$ and the distance r_{OL} is 0.89 Å. As a result, its quadrupole moment differs on average by 18% from the experimental value. Its poor performance on liquid phase properties like the isothermal compressibility or the heat capacity, where it deviates by 20−35% from the experimental evidence, are additional reasons, why we do not discuss this attempt any further.

(68) Wang, L.-P.; Chen, J.; Van Voorhis, T. Systematic Parametrization of Polarizable Force Fields from Quantum Chemistry Data. *J. Chem. Theory Comput.* **2012**, *9*, 452−460.

(69) Verhoeven, J.; Dymanus, A. Magnetic Properties and Molecular Quadrupole Tensor of the Water Molecule by Beam-Maser Zeeman Spectroscopy. *J. Chem. Phys.* **1970**, *52*, 3222−3233.

(70) Dyke, T. R.; Mack, K. M.; Muenter, J. S. The Structure of Water Dimer from Molecular Beam Electric Resonance Spectroscopy. *J. Chem. Phys.* **1977**, *66*, 498−510.

(71) Odutola, J. A.; Dyke, T. R. Partially Deuterated Water Dimers: Microwave Spectra and Structure. *J. Chem. Phys.* **1980**, *72*, 5062−5070.

(72) Hill, P. G.; MacMillan, C. R. Virial Equations for Light and Heavy Water. *Ind. Eng. Chem. Res.* **1988**, *27*, 874−882.

(73) Feistela, R.; Wagner, W. A New Equation of State for H_2O Ice Ih. *J. Phys. Chem. Ref. Data* **2006**, *35*, 1021−1047.

(74) Krynicki, K.; Green, C.; Sawyer, D. Pressure and Temperature Dependence of Self-Diffusion in Water. *Faraday Discuss. Chem. Soc.* **1978**, *66*, 199−208.

(75) Harris, K.; Woolf, L. Temperature and Volume Dependence of the Viscosity of Water and Heavy Water at Low Temperatures. *J. Chem. Eng. Data* **2004**, *49*, 1064−1069.

(76) Weast, R. C. *Handbook of Chemistry and Physics*; CRC: Boca Raton, FL, 1983.

(77) Motakabbir, K. A.; Berkowitz, M. Isothermal Compressibility of SPC/E Water. *J. Phys. Chem.* **1990**, *94*, 8359−8362.

(78) Sprik, M. Hydrogen Bonding and the Static Dielectric Constant in Liquid Water. *J. Chem. Phys.* **1991**, *95*, 6762−6769.

(79) Neumann, M. Dipole Moment Fluctuation Formulas in Computer Simulations of Polar Systems. *Mol. Phys.* **1983**, *50*, 841−858.

(80) Smith, P. E.; van Gunsteren, W. F. Consistent Dielectric Properties of the Simple Point Charge and Extended Simple Point Charge Water Models at 277 and 300 K. *J. Chem. Phys.* **1994**, *100*, 3169−3174.

(81) Tironi, I. G.; Van Gunsteren, W. F. A Molecular Dynamics Simulation Study of Chloroform. *Mol. Phys.* **1994**, *83*, 381−403.

(82) Mahoney, M.; Jorgensen, W. A Five-Site Model for Liquid Water and the Reproduction of the Density Anomaly by Rigid, Nonpolarizable Potential Functions. *J. Chem. Phys.* **2000**, *112*, 8910−8922.

(83) Fernández, R. G.; Abascal, J. L.; Vega, C. The Melting Point of Ice I for Common Water Models Calculated from Direct Coexistence of the Solid-Liquid Interface. *J. Chem. Phys.* **2006**, *124*, 144506.

(84) Gladich, I.; Roeselová, M. Comparison of Selected Polarizable and Nonpolarizable Water Models in Molecular Dynamics Simulations of Ice Ih. *Phys. Chem. Chem. Phys.* **2012**, *14*, 11371−11385.

(85) Klähn, M.; Mathias, G.; Kötting, C.; Schlitter, J.; Nonella, M.; Gerwert, K.; Tavan, P. IR Spectra of Phosphate Ions in Aqueous Solution: Predictions of a DFT/MM Approach Compared with Observations. *J. Phys. Chem. A* **2004**, *108*, 6186−6194.

(86) Schultheis, V.; Reichold, R.; Schropp, B.; Tavan, P. A Polarizable Force Field for Computing the Infrared Spectra of the Polypeptide Backbone. *J. Phys. Chem. B* **2008**, *112*, 12217−12230.

(87) VandeVondele, J.; Tröster, P.; Tavan, P.; Mathias, G. Vibrational Spectra of Phosphate Ions in Aqueous Solution Probed by First-Principles Molecular Dynamics. *J. Phys. Chem. A* **2012**, *116*, 2466−2474.

(88) Jorgensen, W.; Chandrasekhar, J.; Madura, J.; Impey, R.; Klein, M. Comparison of Simple Potential Functions for Simulating Liquid Water. *J. Phys. Chem.* **1983**, *79*, 926−935.

(89) Baranyai, A.; Kiss, P. Polarizable Model of Water with Field-Dependent Polarization. *J. Chem. Phys.* **2011**, *135*, 234110.

(90) Becke, A. D. A New Mixing of Hartree-Fock and Local Density-Functional Theories. *J. Chem. Phys.* **1993**, *98*, 1372−1377.

(91) Lee, C.; Yang, W.; Parr, R. G. Development of the Colle-Salvetti Correlation Energy Formula into a Functional of the Electron Density. *Phys. Rev. B* **1988**, *37*, 785−789.

1602

dx.doi.org/10.1021/jp4125765 | *J. Phys. Chem. B* 2014, 118, 1589−1602